nature communications

Article

https://doi.org/10.1038/s41467-025-66242-5

Understanding oxygen transfer on ceria with Pt single atoms for surface reaction

Received: 2 July 2025

Accepted: 3 November 2025

Published online: 09 January 2026

Check for updates

Yunji Choi[1,5], Seokhyun Choung[2,5], Jaebeom Han[3,5], Jae-eon Hwang[1], Hyeon Jin[1], Yunkyung Kim[2], Jeongjin Kim[4], Jeong Young Park[3] ✉, Jeong Woo Han[2] ✉ & Hyunjoo Lee[1] ✉

Reducible metal oxides are widely used in surface reactions, primarily due to their ability to activate and transfer oxygen. Ceria, known for its rapid Ce^{3+}/Ce^{4+} redox property, is well-known to follow Mars van Krevelen mechanism. In this study, we prepare Pt/CeO_2-Al_2O_3 catalysts with different ceria domain sizes of 3.7, 5.6, and 7.3 nm to understand oxygen transfer, mainly O_2 activation and lattice oxygen transfer. The ceria domains are isolated on the alumina, preventing oxygen transfer between the ceria. Pt single atomic structures are meticulously prepared to exclude O_2 activation on Pt nanoparticles and provide uniform active sites. Interestingly, the activity trend for CO oxidation is reversed in O_2-rich and O_2-deficient conditions. O_2 activation occurs efficiently in small ceria domains of 3.7 nm. In contrast, larger ceria domains exhibit less O_2 activation but significant lattice oxygen transfer. This behavior is also modeled using large-scale molecular dynamics simulations with a neural network potential trained on first-principles data. Based on these understanding, the catalyst for methane oxidation is proposed by accelerating O_2 activation in O_2-rich condition. This work provides an impactful platform for understanding metal oxide catalysts.

A heterogeneous catalytic reaction involves adsorption of reactants, surface reaction, and desorption of products. The lattice components of the catalysts could be involved in the product formation, which is widely acknowledged as Mars van Krevelen (MvK) mechanism[1,2]. The reductive reactant is oxidized by the lattice oxygen species and forms products, which are subsequently desorbed from the surface. The generated oxygen vacancy sites are replenished by the activation of gaseous O_2 and lattice oxygen diffusion. This mechanism indicates that understanding oxygen transfer in metal oxide is crucial for accelerating the catalytic process.

Ceria (CeO_2) has been evidenced to follow MvK mechanism, with its ability to undergo a swift and reversible reduction and oxidation process, coupled with its capacity to facilitate oxygen transfer. When ceria is subjected to a reducing atmosphere, it forms oxygen-deficient CeO_{2-x}, maintaining its fluorite structure even after the loss of oxygen from its lattice and the generation of oxygen vacancies[3]. Subsequently, CeO_{2-x} can be reoxidized to CeO_2 upon exposure to an oxidizing environment. This circular transformation of Ce^{3+}/Ce^{4+} redox couple allows ceria to store and release oxygen in a reversible manner[4,5]. This distinctive redox behavior renders ceria attractive as both a catalyst and a catalyst support for heterogeneous reactions.

The surface atomic arrangements and ceria domain sizes are closely linked with the reducibility of ceria[6–9]. The ability of ceria to form oxygen vacancies refers to its oxygen release and uptake ability during reactions. In particular, the oxygen transfer from ceria plays a decisive role in altering activity, as ceria is perceived to provide oxygen

[1]Department of Chemical and Biomolecular Engineering, Korea Advanced Institute of Science and Technology, Daejeon, Republic of Korea. [2]Department of Materials Science and Engineering, Research Institute of Advanced Materials, Seoul National University, Seoul, Republic of Korea. [3]Department of Chemistry, Korea Advanced Institute of Science and Technology, Daejeon, Republic of Korea. [4]Pohang Accelerator Laboratory, Pohang University of Science and Technology, Pohang, Republic of Korea. [5]These authors contributed equally: Yunji Choi, Seokhyun Choung, Jaebeom Han. ✉e-mail: jeongypark@kaist.ac.kr; jwhan98@snu.ac.kr; azhyun@kaist.ac.kr

to drive the reaction[10–12]. The oxygen transfer ability of ceria can be classified into two categories: O_2 activation and lattice oxygen transfer. We denote the uptake of gaseous oxygen and the replenishment of the oxygen vacancies at the surface as "O_2 activation", while the transfer of oxygen from surface to subsurface or vice versa is denoted as "lattice oxygen transfer". It was reported that O_2 activation depends on the partial pressure of gaseous oxygen and the number of oxygen vacancies on the ceria surface, and lattice oxygen transfer reflects the exchange of surface oxygen species and subsurface oxygen species in ceria[13–15]. However, these terms have often been used interchangeably in heterogeneous catalysis without clear classification.

In this study, we prepared Pt single atomic catalysts on ceria of various sizes deposited on alumina (Pt/CeO_2-Al_2O_3). Since the ceria domain was isolated on non-reducible alumina support, the effect of ceria domain size could be evaluated on oxygen transfer. The single atomic structure of Pt allowed us to exclude O_2 activation by Pt nanoparticles. Using CO oxidation as a probe reaction, we observed that activity varied significantly depending on ceria domain size and reactant compositions. By measuring O_2 and CO uptakes, we were able to decouple O_2 activation from lattice oxygen transfer, explaining the observed activity changes. Ambient-pressure X-ray photoelectron spectroscopy (AP-XPS) was performed to observe changes on the ceria surface during the reaction. The models for molecular dynamics simulations were suggested to further elucidate oxygen transfer on the ceria. Based on these findings, we could design a methane oxidation catalyst with enhanced activity by accelerating O_2 activation.

Results

Formation of single atomic Pt on CeO_2 domains with different sizes

Pt catalysts were deposited on CeO_2-Al_2O_3 support (Pt 0.1 wt% and CeO_2 10 wt%) by dispersing cerium and Pt precursors in an alumina suspension, drying, calcining, and reducing them at 300 °C. The Pt single atomic structure was obtained by re-dispersion under N_2 purging at 600 °C. The size of ceria domains was controlled by changing the calcination temperature to 500, 600, and 700 °C. When the ceria domain size was estimated from X-ray diffraction pattern (XRD), it was 3.7 nm, 5.6 nm, and 7.3 nm, respectively (Supplementary Fig. 1). We denote the Pt/CeO_2-Al_2O_3 catalysts as XCA with X representing the size of ceria domain. When the catalyst was synthesized without alumina, it is denoted as Pt/CeO_2 and the ceria domain size was 27.6 nm. Pt nanoparticle catalyst was also prepared by depositing 0.1 wt% Pt on alumina and it is denoted as Pt NP/Al_2O_3. The detailed synthesis procedure is described in "Methods" section.

High-angle annular dark-field scanning transmission electron microscopy (HAADF-STEM) images confirmed that different sizes of ceria domains were isolated on alumina support in the CA catalysts, whereas ceria domains were overlapped in Pt/CeO_2 (Fig. 1). X-ray photoelectron spectroscopy (XPS) Ce 3*d* spectra showed that the fraction of Ce^{3+} was 34.9%, 29.3%, 26.5%, and 24.8% in 3.7CA, 5.6CA, 7.3CA, and Pt/CeO_2, respectively (Supplementary Fig. 2). As the ceria domain size became larger, the surface defect sites decreased.

In order to analyze the effect of ceria domain size for surface reaction and exclude the effect of various Pt surface structures, the Pt structure was controlled to possess the single atomic configuration, since precious metal nanoparticles can easily activate gaseous oxygen[16,17]. Only 0.1 wt% of Pt was deposited and its content was confirmed through inductively coupled plasma (ICP) (Table 1). Pt L_3-edge spectra of extended X-ray absorption fine structure (EXAFS) revealed no discernible Pt-Pt scattering peak while exhibiting a Pt-O scattering peak, implying that these catalysts have single atomic Pt structure (Supplementary Fig. 3a). The Pt-O coordination number was 4.38, 4.37, 4.37, and 5.16 for 3.7CA, 5.6CA, 7.3CA, and Pt/CeO_2, respectively (Supplementary Table 1). When Pt dispersion was estimated from H_2 uptake, the Pt dispersion was nearly 100% in these four samples

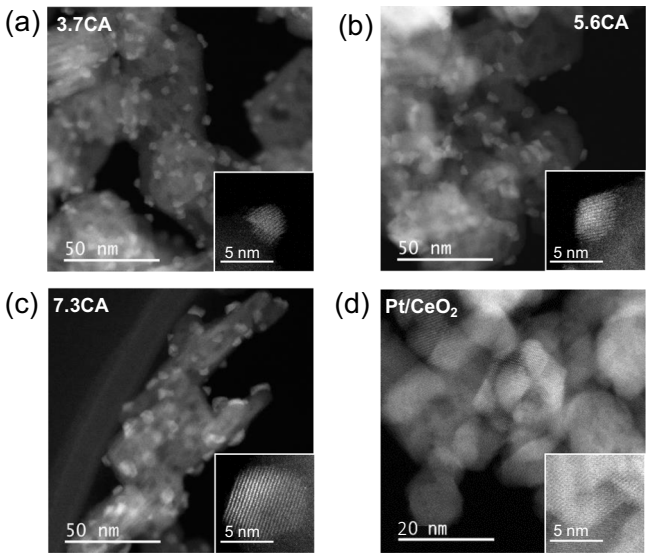

Fig. 1 | Morphology of single atomic Pt/CeO_2-Al_2O_3 with different ceria sizes and Pt/CeO_2. The Pt content was 0.1 wt% in all cases. **a**–**d** HAADF-STEM images of 3.7CA, 5.6CA, 7.3CA, and Pt/CeO_2, respectively. The number represents the ceria domain size in nm.

(Table 1). CO-diffuse reflectance infrared Fourier-transform spectra (CO-DRIFTS) exhibited a single peak at 2087 cm^{-1} for 3.7CA, 5.6CA, and 7.3CA, assigned to linear CO adsorbed on single atomic Pt[18–20]. Pt/CeO_2 also presented the linear CO peak at 2090 cm^{-1}, with much smaller peak intensity (Supplementary Fig. 3b). These CO-DRIFTS results confirmed that Pt single atomic structure was formed in 3.7CA, 5.6CA, 7.3CA, and Pt/CeO_2 catalysts. The number of Pt atoms per one ceria domain was estimated to be 2.7, 9.4, 20.8 for 3.7CA, 5.6CA, and 7.3CA, respectively (Table 1).

Ceria domain size-dependent activity for CO oxidation

CO oxidation was conducted under various CO:O_2 ratios to assess the effect of ceria domain size on oxidation. CO oxidation was selected as a probe reaction because it is a relatively simple reaction with well-established mechanisms[21]. When the reaction occurs in O_2-deficient condition (CO:O_2 = 10:1), larger ceria domains exhibited better activity, with the order of activity being 3.7CA < 5.6CA < 7.3CA (Fig. 2a, b). On the other hand, when the reaction occurs in O_2-rich condition (CO:O_2 = 1:1 or 1:10), the trend in activity reversed, with the order of 3.7CA > 5.6CA > 7.3CA (Fig. 2c–f). Pt/CeO_2 and Pt NP/Al_2O_3 displayed at most comparable or much lower activity in all the conditions. Clearly, the activity of Pt/CeO_2-Al_2O_3 catalysts depended on the size of the ceria domain and reactant composition. CO-DRIFTS was conducted for 3.7CA after the reaction under various CO:O_2 ratios to exclude the possibility that a change in the Pt structure might contribute to the activity difference. The Pt structure remained as single atomic after the reaction, indicated by no discernible peak shift (Supplementary Fig. 4). When the shift of CO peak was also monitored by switching CO and O_2 flow, the shift was hardly observed in all the catalysts (Supplementary Fig. 5). To understand the underlying reasons of the reversal in activity trend upon the change from O_2-deficient to O_2-rich condition and how the size of ceria domain exerts influence, further characterizations of the catalysts were conducted.

Oxygen transfer in the ceria domain with various sizes

First, reaction kinetics study was performed on CO oxidation. The reaction orders in CO were found to be 1.08, 1.08, 1.06, and 1.01 and the reaction orders in O_2 were 0.01, 0.02, 0.01, and 0.03 for 3.7CA, 5.6CA, 7.3CA, and Pt/CeO_2, respectively, under O_2-deficient condition (CO partial pressure of 1.5 kPa and O_2 partial pressure of 0.3-0.7 kPa;

https://doi.org/10.1038/s41467-025-66242-5

Table 1 | Properties of single atomic Pt/CeO_2-Al_2O_3 (CA) with various ceria domain sizes, Pt/CeO_2, and Pt NP/Al_2O_3 catalysts

	Ceria domain size[a] (nm)	BET surface area (m^2 g_{cat}^{-1})	Pt content[b] (wt%)	Pt dispersion[c] (%)	Number of Pt atom per one ceria domain[d]
3.7CA	3.7	49.7	0.1	100.4	2.7
5.6CA	5.6	47.2	0.1	100.0	9.4
7.3CA	7.3	45.0	0.1	101.3	20.8
Pt/CeO_2	27.6	22.0	0.1	100.7	112.4
Pt NP/Al_2O_3	-	51.3	0.1	54.8	-

[a]Estimated based on Scherrer equation from CeO_2(111) peak at 28.5°.
[b]Measured by ICP.
[c]Measured by H_2 uptake.
[d]The detailed procedure for estimation was explained in the supplementary information.

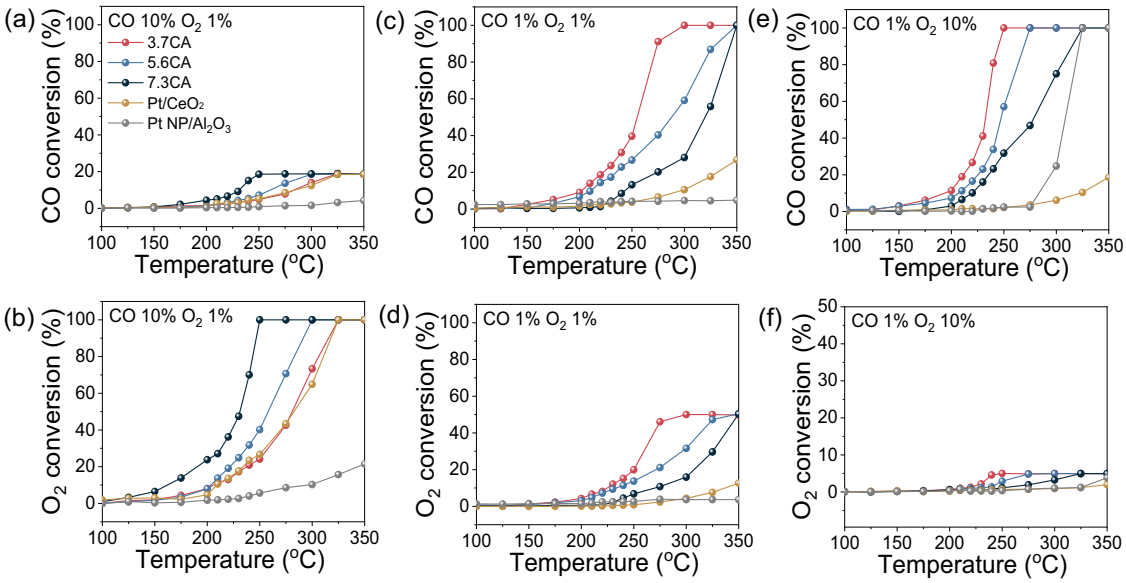

Fig. 2 | CO oxidation performance on single atomic Pt/CeO_2-Al_2O_3 with different ceria domain sizes, Pt/CeO_2, and Pt NP/Al_2O_3. **a** CO and **b** O_2 conversion in CO 10%, O_2 1% with He balance. **c** CO and **d** O_2 conversion in CO 1%, O_2 1% with He balance. **e** CO and **f** O_2 conversion in CO 1%, O_2 10% with He balance.

Fig. 3a, b). This observation of positive order in CO and zero order in O_2 points to Mars-van Krevelen (MvK) mechanism, generally reported for ceria-based catalysts[22–25]. In the MvK mechanism, CO adsorbed on Pt site reacts with a surface oxygen of nearby ceria, forming CO_2. The CO_2 desorbs, leaving oxygen vacancy. The oxygen vacancy can be replenished by lattice oxygen transfer, which provides zero order in O_2[26]. In the case of Pt NP/Al_2O_3, the reaction order in CO was −0.23 and the order in O_2 was 0.93, referring to the Langmuir-Hinshelwood mechanism, in which both CO and O_2 adsorb on the Pt surface to form CO_2. We additionally measured the reaction order in O_2 under O_2-rich condition (CO partial pressure of 1.5 kPa and O_2 partial pressure of 3–3.4 kPa; Fig. 3c). The reaction order in O_2 became more positive with the values of 0.16, 0.24, 0.33, and 0.39 for 3.7CA, 5.6CA, 7.3CA, and Pt/CeO_2, respectively. The oxygen vacancy can be also replenished by gaseous O_2 in this O_2-rich condition. The larger ceria domain exhibited the larger reaction order in O_2, implying more difficult O_2 activation.

The observed difference in the activity for various ceria domain sizes (Fig. 2) could potentially be explained by the difference in their oxygen transfer capabilities. O_2-temperature programmed desorption (O_2-TPD) results show that 3.7CA had the largest amount of adsorbed surface oxygen species, which presents the peaks at the temperatures below 500 °C (Supplementary Fig. 6a). H_2-temperature programmed reduction (H_2-TPR) results of Pt/CeO_2-Al_2O_3 catalysts show two reduction peaks at ~370 °C and ~630 °C, indicating the reduction of surface oxygen and subsurface oxygen species, respectively (Supplementary Fig. 6b). It was expected that surface oxygen vacancies would be formed after H_2 pretreatment at 550 °C while subsurface oxygen vacancies would be formed after the treatment at 750 °C. In a case of Pt/CeO_2, the subsurface oxygen was reduced at higher temperature, so the reduction was performed at 900 °C instead of 750 °C. Then O_2 uptakes were estimated by measuring the changes in O_2 pulses to observe how many O_2 molecules were taken by the catalysts with oxygen vacancies. The O_2 uptakes normalized by ceria surface area are shown in the main text, while the raw data and the value normalized by total catalyst mass are shown in the supplementary information (Supplementary Figs. 7–9).

Interestingly, the O_2 uptakes for the catalysts reduced at two different temperatures presented the opposite trend. As the ceria domain size increased, the amount of O_2 uptake decreased when the ceria was reduced at 550 °C (1.5, 0.64, 0.57, and 0.1 μmol m_{ceria}^{-2} for 3.7CA, 5.6CA, 7.3CA, and Pt/CeO_2), but it increased when the ceria was reduced at 750 °C (1.7, 4.6, 7.3, and 15.6 μmol m_{ceria}^{-2} for 3.7CA, 5.6CA, 7.3CA, and Pt/CeO_2) (Fig. 3d and e). The difference in the O_2 uptakes, which was denoted with patterned color in Fig. 3e, became larger for larger ceria. We think that the O_2 uptakes measured after the reduction at 550 °C indicate O_2 activation on the surface oxygen vacancies, which is proportional to the Ce^{3+} fraction (Fig. 3d scheme). On the other hand, the O_2 uptakes measured after deeper reduction at 750 °C further included both O_2 activation and lattice oxygen transfer into the sub-surface oxygen vacancies (Fig. 3g). Whereas O_2 activation occurred more as the ceria domain size decreased, lattice oxygen transfer occurred more as the ceria domain size increased. XRD, HAADF-STEM,

https://doi.org/10.1038/s41467-025-66242-5

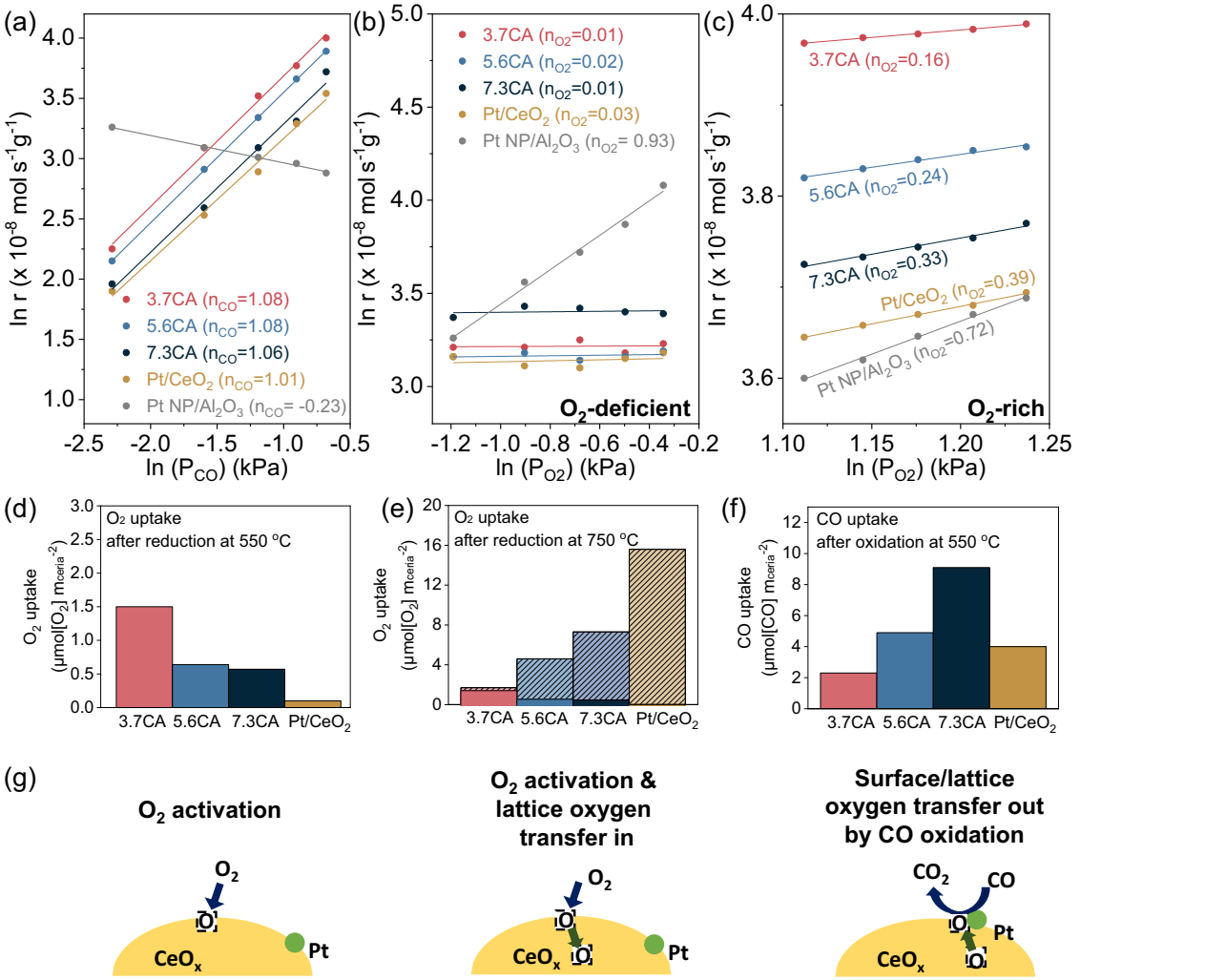

Fig. 3 | Study of oxygen transfer by reaction kinetics and uptakes of O_2 and CO. Reaction rate as a function of (**a**) CO or (**b**, **c**) O_2 partial pressure. The O_2 partial pressure was 0.5 kPa in (**a**). CO partial pressure was 1.5 kPa in (**b**, **c**) while (**b**) was measured in O_2-deficient condition (P_{O2} = 0.3-0.7 kPa) and (**c**) was measured in O_2-rich condition (P_{O2} = 3–3.4 kPa). Reaction orders (n_{CO} or n_{O2}) are estimated from the slopes of linear fitting. O_2 uptakes at 500 °C normalized by ceria surface area and illustration of O_2 uptake process obtained after H_2 pretreatment at (**d**) 550 °C and (**e**) 750 °C. Pt/CeO_2 was reduced at 900 °C instead of 750 °C. The patterned color represents the difference in the O_2 uptakes after H_2 pretreatment at 550 °C and 750 °C. **f** CO uptake at 500°C normalized by ceria surface area. **g** Illustration of O_2 and CO uptake processes of (**d**–**f**).

and CO-DRIFTS results obtained after the O_2 uptake measurements confirmed that the ceria domain size or Pt atomic configuration were barely changed (Supplementary Figs. 10–12).

These differences in O_2 uptakes explain the opposite activity trends under different gas environments. In O_2-rich condition of CO oxidation (CO:O_2 = 1:1 or 1:10; Fig. 2c-f), O_2 activation occurs more effectively on smaller ceria domain, and the abundant gaseous O_2 feed can facilitate the replenishment of surface oxygen vacancies. In O_2-deficient condition (CO:O_2 = 10:1; Fig. 2a and b), the replenishment of surface oxygen vacancies with gaseous O_2 may be insufficient; instead the diffusion of lattice oxygen from the inner layers to the surface may exert more influence on the activity. Hence, larger ceria with more transferrable subsurface oxygen can demonstrate higher activity.

To further validate these results, we performed oxygen isotope experiments using CO and $^{18}O_2$ at 200 °C under both O_2-deficient (CO 7 kPa, $^{18}O_2$ 0.7 kPa) and O_2-rich (CO 0.7 kPa, $^{18}O_2$ 0.7 kPa) conditions (Fig. 4a and b). Mass spectrometry detected $C^{16}O^{16}O$, $C^{16}O^{18}O$, and $C^{18}O^{18}O$, and the reaction pathways were schematically summarized. CO first adsorbs on Pt and reacts with neighboring lattice ^{16}O in ceria, producing $C^{16}O^{16}O$ and leaving behind an oxygen vacancy. The vacancy can be replenished by lattice ^{16}O transfer and form $C^{16}O^{16}O$ more (Fig. 4c). This vacancy can be also replenished by gaseous $^{18}O_2$ activation or lattice ^{18}O transfer, leading to the subsequent formation of $C^{16}O^{18}O$ (Fig. 4d). CO adsorbed on Pt can exchange oxygen with ^{18}O, and this $C^{18}O$ can react with neighboring ^{18}O from ceria, forming $C^{18}O^{18}O$ (Fig. 4e). Under O_2-deficient condition, 3.7CA showed a gradual decrease in the production of $C^{16}O^{16}O$ and increase in $C^{16}O^{18}O$, because surface ^{16}O in ceria was consumed and the surface oxygen vacancy was replenished by ^{18}O. In 7.3CA, however, $C^{16}O^{16}O$ formation initially increased because the lattice ^{16}O was provided to the surface more than 3.7CA. Under O_2-rich condition, 3.7CA showed rapid decay of $C^{16}O^{16}O$ and growth of $C^{16}O^{18}O$, consistent with fast O_2 activation at abundant surface vacancies, whereas 7.3CA exhibited lower overall CO_2 formation. These isotope results also support that larger ceria domains are more effective in supplying lattice oxygen under O_2-deficient condition, while smaller domains favor surface O_2 activation under O_2-rich condition.

The CeO_2-Al_2O_3 supports were synthesized without Pt single atoms. When the supports were calcined without Pt precursor at 500, 600, and 700 °C, the ceria domain size was 7.1, 7.1, and 7.3 nm, respectively. The absence of Pt caused ceria sintering[20]. The effect of Pt single atom on O_2 uptakes was evaluated for the 7.3 nm samples in the

https://doi.org/10.1038/s41467-025-66242-5

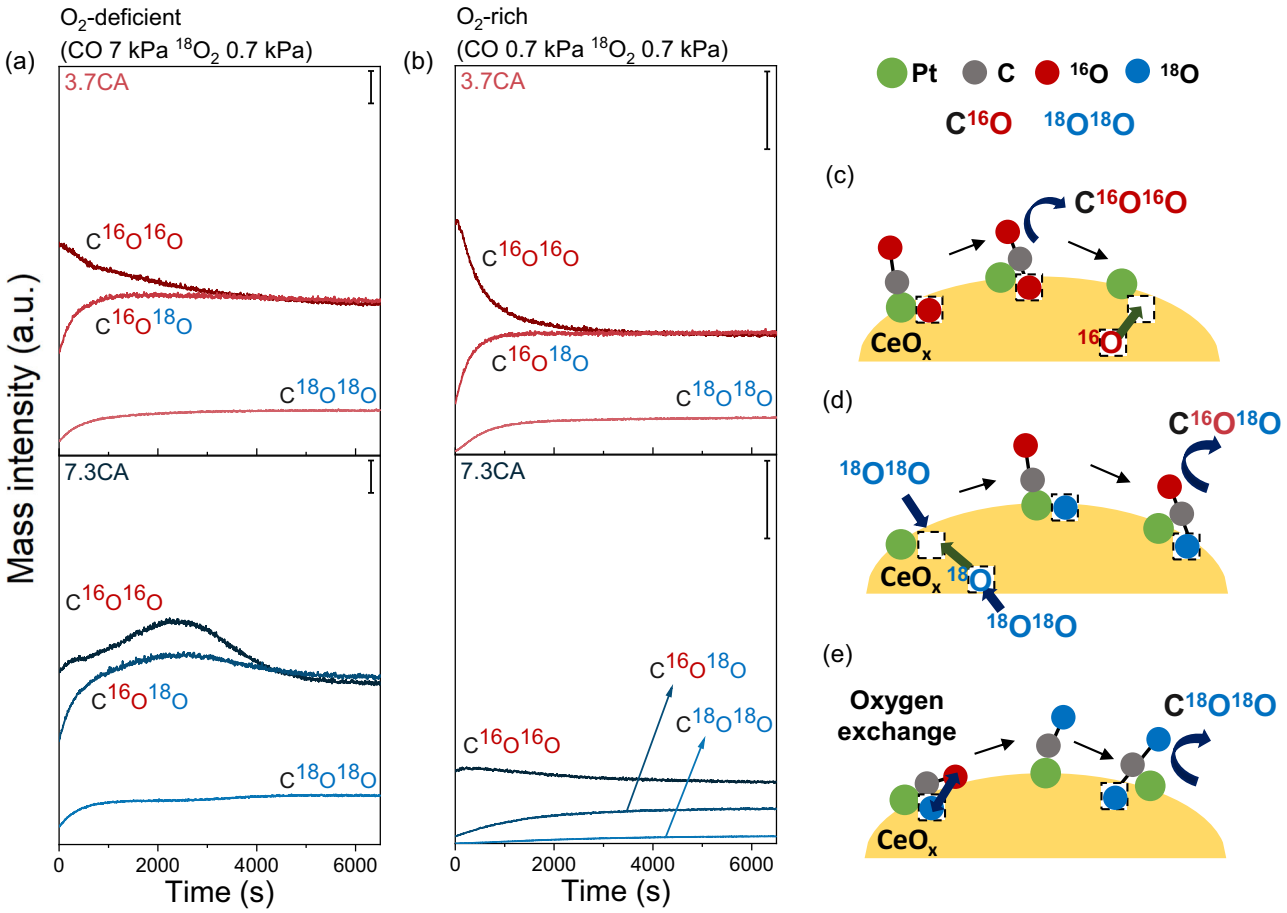

Fig. 4 | Oxygen isotope experiment under different reaction conditions. The experiments were measured at 200 °C on 3.7CA and 7.3CA under **a** O_2-deficient condition (CO 7 kPa, $^{18}O_2$ 0.7 kPa with He balance) and **b** O_2-rich condition (CO 0.7 kPa, $^{18}O_2$ 0.7 kPa with He balance). Scheme of **c** $C^{16}O^{16}O$, **d** $C^{16}O^{18}O$, **e** $C^{18}O^{18}O$ formation under oxygen isotope experiment.

presence and absence of Pt single atoms (Supplementary Fig. 13). The O_2 uptakes were the same regardless of Pt, indicating that O_2 uptakes do not occur on the single atomic Pt sites.

CO uptakes are often used to estimate oxygen storage capacity[4,27,28]. After the catalysts were pre-treated with O_2 at 550 °C, CO uptakes were estimated by measuring the changes in CO pulses (Fig. 3f and Supplementary Fig. 14). The CO would adsorb on Pt site, then react with neighboring oxygen, leaving oxygen vacancy behind after CO_2 desorbs. Then, the oxygen vacancy would be replenished by lattice oxygen transfer (Fig. 3g; right scheme). As the ceria domain size increased, the CO uptake also increased except for Pt/CeO_2. This is similar to the O_2 uptake results obtained after the reduction at 750 °C, representing the outward transfer of surface and lattice oxygen by CO oxidation. The CO uptake of the Pt/CeO_2 was lower than that of the 7.3CA. The Pt-O coordination number is 5.16 in the Pt/CeO_2, while the number is lower as ~4.4 in the CA catalysts. The higher coordination of Pt with neighboring oxygen may retard oxygen transfer slightly. The O_2 and CO uptake were also measured for the Pt NP/Al_2O_3, but the values were much smaller than those of the ceria-based catalysts (Supplementary Fig. 9).

Ambient-pressure XPS measurements

In order to understand the oxygen transfer behavior by controlling ceria domain size, it is imperative to monitor the catalytic surface under reaction conditions with surface-sensitive techniques. In this case, the nature of the alumina-based catalyst led to severe charging shift, which were especially pronounced under oxidizing conditions. Consequently, we chose a strategy focusing on the CO:O_2 = 1:1 and 10:1, rather than 1:10 conditions. The measurements under the O_2-rich condition (CO:O_2 = 1:1) were conducted using lab-based AP-XPS with Al K-α X-ray source by increasing the temperature from room temperature to 100, 200, and 300 °C (Supplementary Fig. 15). The Ce^{3+} area ratio difference between three samples remains consistent with increasing temperature. The increase in the Ce^{3+} area ratio with the temperature under O_2-rich conditions is attributed to the amount of oxygen consumed for CO oxidation exceeding the rate at which surface vacancies are healed. The 3.7CA presented the highest Ce^{3+} area ratio in all the temperatures, ensuring its high O_2 activation ability.

We conducted synchrotron-based AP-XPS measurement under O_2-deficient condition (CO:O_2 = 10:1) to investigate oxygen transfer ability more precisely (Fig. 5a-c). A photon energy of 1050 eV was used to conduct surface-sensitive analysis, resulting in a probing depth of ~1.6 nm. The Ce^{3+} area ratio at room temperature was the highest at 41.6% for 3.7CA, 38.1% for 5.6CA, and 32.0% for 7.3CA. Interestingly, under O_2-deficient condition, the Ce^{3+} area ratio for 7.3CA increased significantly as the temperature rose from 32.0% at room temperature to 49.4% at 300 °C. For 3.7CA, the Ce^{3+} area ratio showed a subtle increase from 41.6% at room temperature to 44.2% at 300 °C, leading to a reversal of Ce^{3+} area ratios at 300 °C (Fig. 5d). This reversal in Ce^{3+} area ratio at higher temperatures is attributed to the CO oxidation under conditions where O_2 activation is constrained. These findings suggest that substantial subsurface oxygen was consumed via lattice oxygen transfer during CO oxidation, which aligns with the superior CO oxidation activity of 7.3CA under O_2-deficient condition. This observation is also consistent with our uptake results: smaller ceria domains favor surface O_2 activation, while larger ceria domains experience more lattice oxygen transfer.

https://doi.org/10.1038/s41467-025-66242-5

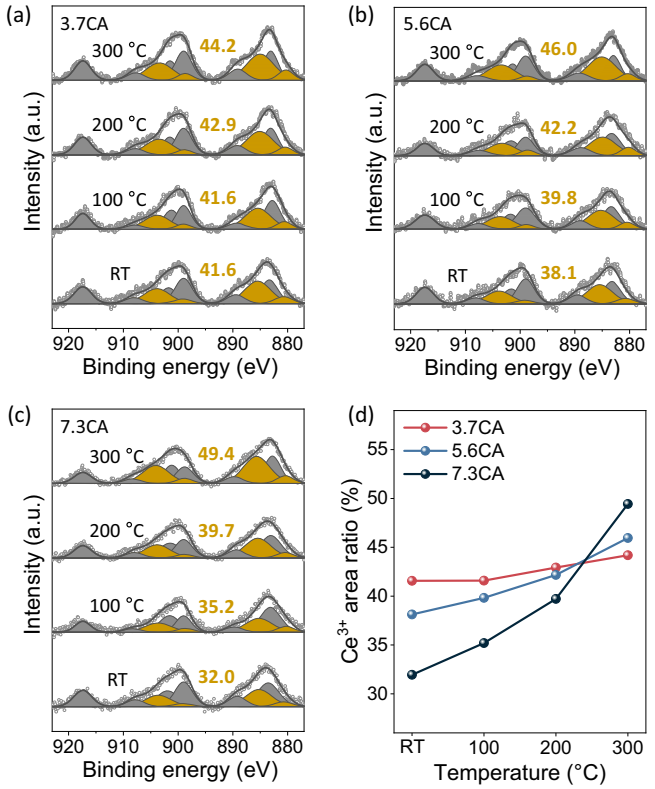

Fig. 5 | Synchrotron-based ambient-pressure XPS under O_2-deficient condition. Ce 3*d* spectra obtained under CO:O_2 = 10:1 (CO 0.03 mbar, O_2 0.003 mbar) at elevated temperatures for **a** 3.7CA, **b** 5.6CA, and **c** 7.3CA. **d** Ce^{3+} area ratios estimated from the peak deconvolution.

Molecular dynamics simulations of the ceria domains for O_2 uptake

To further understand the effect of ceria domain size on oxygen activation and diffusion kinetics observed in O_2 uptake experiment, we performed large scale molecular dynamics (MD) simulations using three Pt/CeO_2-Al_2O_3 models with different ceria domain sizes. Classical force field-based molecular dynamics (MD) simulations are not suitable for our model system due to their limited accuracy, while electronic structure methods such as density functional theory (DFT), despite their accuracy, struggle with scalability to extended length and time scales. To overcome these limitations, we have employed a state-of-the-art neural network potential (NNP) model. This computational framework allows for a systematic exploration of large-scale ceria domains through extensive MD simulations under experimental conditions, without sacrificing precision.

The thermodynamically stable Pt/CeO_2-Al_2O_3 models were constructed by performing annealing MD simulations of three hemisphere ceria models on Al_2O_3 slab, where each model represents ceria domain sizes of 3.7CA, 5.6CA, and 7.3CA. Followed by annealing MD simulations, Pt single atoms were anchored on ceria domains, and surface Ce^{3+} sites were generated by removing surface oxygen atoms to have the Ce^{3+} ratio of 40%, 30%, and 30% for 3.7CA, 5.6CA, and 7.3CA, respectively, reflecting XPS data (Supplementary Figs. 16–18). O_2 uptake MD simulations were conducted using these three Pt/CeO_2-Al_2O_3 models in O_2 gas randomly distributed in the simulation boxes (Fig. 6a and Supplementary Fig. 19). To ensure a comprehensive exploration of the configuration space, five O_2 gas configurations were used. All simulations reached thermodynamic equilibrium and exhibited exothermic changes (Supplementary Fig. 20).

O_2 uptake can be primarily divided into two sequential processes: O_2 activation and lattice oxygen transfer. O_2 activation involves the surface activation of gaseous oxygen, whereas lattice oxygen transfer involves the sequential transfer of activated oxygen species from the surface to the subsurface region of the ceria domain (Fig. 6b, c). In the case of O_2 activation, different types of activated oxygen species were observed, including filling of surface Ce^{3+} sites, surface physisorption, coordination with Pt, and chemisorption on the lattice oxygen (Supplementary Fig. 21a and b). These configurations of activated oxygen species on the surface were observed regardless of the ceria domain sizes (Fig. 6b). Following O_2 activation, we observed transfer of the activated surface oxygen species into the subsurface region and further transfer into the bulk region of the ceria domain (Supplementary Fig. 21c and Fig. 6c).

To quantify the O_2 uptake within the ceria domains, the change in Ce-O coordination number of all Ce atoms in each model was monitored during the MD simulations. We classified all Ce atoms in the system as either surface Ce atoms or bulk Ce atoms based on their oxygen coordination (see Supplementary Information and Supplementary Fig. 22 for details). The changes in Ce-O coordination of surface Ce atoms were assigned to O_2 activation, while those of bulk Ce atoms to lattice oxygen transfer. The statistical uncertainties shown as error bars are relatively small, indicating that O_2 uptake MD simulations were independent of the initial O_2 gas configurations. In the 7.3CA model, a notable decrease in O_2 activation was observed from 1.39 $\mu mol[O_2]/m_{ceria}^2$ at 25 ps to 1.18 $\mu mol[O_2]/m_{ceria}^2$ at 100 ps, indicating that activated gaseous oxygen is diffused from the surface into the bulk region (Fig. 6d). In smaller ceria domains, O_2 uptake predominantly occurs at the surface (85% O_2 activation vs. 15% lattice oxygen transfer for 3.7CA) (Fig. 6e). As the size of the ceria domains increases, a greater proportion of lattice oxygen transfer is observed (46% and 51% for 5.6CA and 7.3CA, respectively), indicating a size-dependent trend in oxygen activation and lattice oxygen transfer dynamics. These trends are consistent with experimental observation of Fig. 3e.

The effect of undercoordinated surface Ce^{3+} sites density was further investigated on the various ceria domain sizes. Experimentally, the smaller ceria domain tends to have larger Ce^{3+} sites and it is very difficult to distinguish the Ce^{3+} sites density effect from the size effect. To systematically analyze the effect of the surface Ce^{3+} defect site density while isolating the effect of ceria domain size, we constructed additional six theoretical models by adjusting the number of surface oxygen atoms. This resulted in a total of nine models: 3.7CA, 5.6CA, and 7.3CA models, each with the stoichiometric Ce^{3+} ratio of 20%, 30%, and 40% (Fig. 6f). This approach allowed us to isolate the effects of Ce^{3+} sites density from ceria domain size (Supplementary Figs. 23 and 24). The total O_2 uptake of 3.7CA model remained relatively constant regardless of the Ce^{3+} ratio, exhibiting minimal variation with increasing Ce^{3+} defect sites density (Fig. 6f). In contrast, larger ceria domains, the 5.6CA and 7.3CA models, demonstrated a progressive increase in O_2 uptake with the presence of more Ce^{3+} defect sites. When O_2 activation and lattice oxygen transfer were separately evaluated (Supplementary Fig. 24), the O_2 activation occurs more at higher Ce^{3+} ratio regardless of the ceria domain size, while large ceria domains facilitate the incorporation of activated O_2 into the ceria lattice, allowing more oxygen to be accommodated in the bulk and subsurface regions.

To explicitly evaluate the role of Pt single atoms in O_2 uptake, the O_2 uptake MD simulations were also performed using CeO_2-Al_2O_3 models without Pt (Supplementary Figs. 25 and 26). Fig. 6g shows the theoretical total O_2 uptakes of Pt/CeO_2-Al_2O_3 models on the *x*-axis and those of CeO_2-Al_2O_3 models on the *y*-axis. The total O_2 uptake remains largely unchanged regardless of the presence of Pt single atoms in the system. Some of the data points are positioned slightly to the right side from the parity line, indicating a subtle increase in O_2 uptake due to the presence of Pt single atom sites. However, the difference was negligibly small compared to the effect of Ce^{3+} site density and ceria domain size. This effectively rules out the role of Pt single atom sites in influencing the O_2 uptake.

https://doi.org/10.1038/s41467-025-66242-5

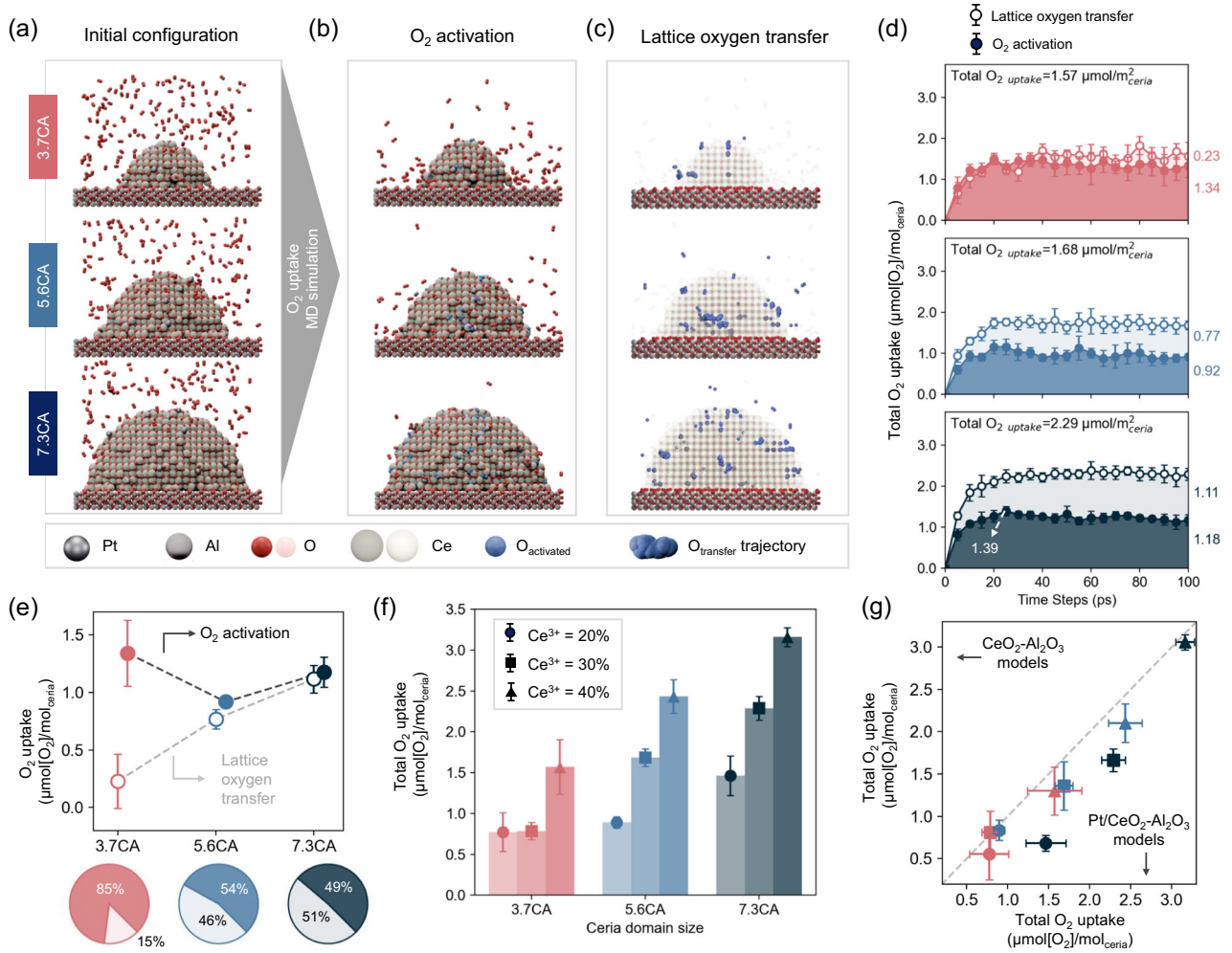

Fig. 6 | Molecular dynamics simulations of three ceria domain sizes for O_2 uptake. a Snapshots of the initial configurations for Molecular dynamics (MD) simulations at 773 K. **b** Final configuration of O_2 activation on the surface of ceria domain after MD. **c** Transfer trajectory of lattice oxygen, where the position of each transferred O atom is indicated in darker blue over the simulation time, plotted every 5 ps. The Ce atoms and other O atoms are displayed transparently. **d** Total O_2 uptake of three ceria domains plotted against the simulation time, where the O_2 uptake is classified into O_2 activation and lattice oxygen transfer. **e** O_2 uptake classified into O_2 activation and lattice oxygen transfer for three ceria domains. The ratio of O_2 activation (dark color) and lattice oxygen transfer (light color) is shown in the pie charts. **f** Total O_2 uptake of three ceria domain sizes for three different Ce^{3+} ratio (20%, 30% and 40%). **g** Total O_2 uptake comparison with and without Pt single atoms in the system. Error bars represent one standard deviation of five repeated simulations (**d**–**g**).

Industrially relevant oxidations

In order to explore the industrial potential of ceria structure modulation, the catalysts with different ceria domain sizes were tested for CH_4 oxidation (Fig. 7a). Because methane oxidation typically occurs at O_2-rich conditions, we can expect that smaller ceria would facilitate O_2 activation based on our findings above. Truly, the activity of CH_4 oxidation showed the order of 3.7CA > 5.6CA > 7.3CA > Pt/CeO_2 > Pt NP/Al_2O_3 for 0.1 wt% Pt. PtPd bimetallic catalysts are generally known to exhibit high activity for methane oxidation, because Pd behaves as active sites via Pd-PdO redox cycles and Pt helps Pd to maintain its electronic state[29,30]. The catalysts with 0.1 wt% Pt and 0.1 wt% Pd were prepared using additional palladium (II) nitrate hydrate (Sigma-Aldrich) without N_2 re-dispersion and tested for methane oxidation (Supplementary Fig. 27 and Fig. 7b). The CH_4 conversion at 300 °C was 69.1%, 53.1%, 34.1%, 8.3%, and 0% in PtPd/3.7CA, PtPd/5.6CA, PtPd/7.3CA, PtPd/CeO_2, and PtPd/Al_2O_3, respectively. Clearly, the smaller ceria domain accelerated CH_4 conversion at low temperatures.

The loading of Pt and Pd in PtPd/CeO_2 catalysts was varied to enhance methane oxidation activity and compared with PtPd/3.7CA containing 0.1 wt% Pt and 0.1 wt% Pd. Although the metal content increased up to 1 wt%, the CeO_2 support presented less activity than the 3.7CA with 0.1 wt% metals (Fig. 7c), demonstrating that controlling the ceria domain size anchored on alumina can be powerful to facilitate O_2 activation in O_2-rich condition. The activity for methane oxidation typically degrades in the presence of moisture. When the methane oxidation was repeated under additional 5% H_2O at otherwise the same condition, the PtPd/3.7CA still presented the highest activity (Fig. 7d). The size of ceria domain was barely changed in the CA samples, while the PtPd/CeO_2 suffered from significant ceria sintering (Supplementary Fig. 28). These findings illustrate that enhancing O_2 activation by controlling the property of ceria support can be an efficient way to promote methane oxidation in O_2-rich condition, while reducing the loading of precious metals.

Discussion

This work provides insights into oxygen transfer on ceria and its impact on surface reactions. We synthesized Pt/CeO_2-Al_2O_3 catalysts with various ceria domain sizes of 3.7, 5.6, and 7.3 nm (denoted as 3.7CA, 5.6CA, and 7.3CA, respectively). Unlike Pt/CeO_2, the ceria domains were isolated on alumina, preventing oxygen transfer between ceria domains and thus allowing an accurate assessment of the effect of ceria domain size. Pt single atomic structures were

https://doi.org/10.1038/s41467-025-66242-5

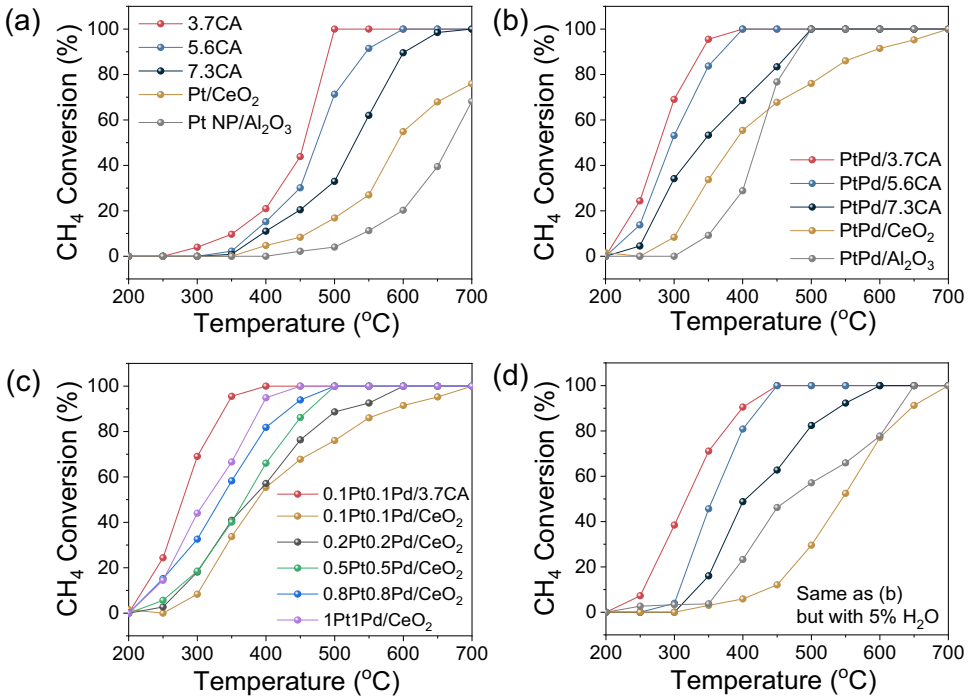

Fig. 7 | Catalytic performance for CH_4 oxidation. CH_4 oxidation on **a** 0.1 wt% Pt deposited on CeO_2-Al_2O_3 with different sizes of ceria domain, CeO_2, and Al_2O_3 with N_2 re-dispersion, **b** 0.1 wt% Pt and 0.1 wt% Pd prepared without N_2 re-dispersion, and **c** various loadings of Pt and Pd on CeO_2 prepared without N_2 re-dispersion. The loading of Pt and Pd was adjusted from 0.1 wt% Pt and 0.1 wt% Pd (0.1Pt0.1 Pd) to 1 wt% Pt and 1 wt% Pd (1Pt1Pd). CH_4 0.1% and O_2 15% (Ar balance) were flown at 10,909 mL g^{-1} h^{-1} and atmospheric pressure. **d** CH_4 oxidation under additional 5% H_2O on 0.1 wt% Pt and 0.1 wt% Pd catalysts.

meticulously prepared to exclude O_2 activation on Pt nanoparticles. When CO oxidation was performed on the Pt/CeO_2-Al_2O_3 catalysts, the activity was highly dependent on ceria domain size and reactant composition. This variation was due to the distinct oxygen transfer properties of O_2 activation and lattice oxygen transfer. We successfully decoupled O_2 activation on ceria from lattice oxygen transfer. The smaller ceria facilitated surface O_2 activation, resulting in high activity under O_2-rich conditions. Conversely, under O_2-deficient conditions, lattice oxygen transfer played a more important role, yielding higher activity in larger ceria domain. Ambient-pressure XPS results showed that under O_2-rich conditions, 3.7CA exhibited the highest Ce^{3+} area ratio at all temperatures. In contrast, under O_2-deficient conditions, larger ceria domains demonstrated a significant change in the Ce^{3+} area ratio as the temperature increased, which is attributed to lattice oxygen transfer capabilities. The size-dependent oxygen kinetics of ceria domains were systematically investigated using large-scale MD simulations of realistic models with a neural network potential trained on first-principles data. The activation of gaseous oxygen and oxygen transfer were monitored and quantified at the atomic level, confirming the effect of ceria domain size and defect site density. PtPd catalyst deposited on small ceria domain presented high activity for methane oxidation due to facilitated O_2 activation in O_2-rich condition. This work highlights the role of understanding oxygen transfer in metal oxide support to enhance catalytic performance.

Methods

Synthesis of single atomic Pt/CeO_2-Al_2O_3 catalysts

γ-Al_2O_3 (99.97%, Alfa Aesar) was calcined at 700 °C. The appropriate amount of cerium nitrates (Kanto chemical, 99.99%) was dissolved in deionized water to prepare 10 wt% of CeO_2 on alumina. The alumina was introduced into the cerium precursor solution and stirred for 1 h. Chloroplatinic acid (Sigma-Aldrich, ≤100%) was dissolved in deionized water to prepare 0.1 wt% Pt and the solution was dropped into a suspension of alumina and a cerium precursor solution. The resulting solution was heated until completely evaporated, ground, and calcined in air at 500, 600, or 700 °C for 5 h. Then the samples were reduced at 300 °C for 1 h under 10% H_2 (N_2 balance), and purged with N_2 flow at 600 °C for 10 h for re-dispersion to prepare Pt single atomic structure[31]. Pt/CeO_2 was prepared using CeO_2 (Sigma Aldrich) by the same method without alumina and cerium precursor. Pt NP/Al_2O_3 was synthesized using polyol method. NaOH (Samchun) 6.12 mg and sodium acetate (Sigma Aldrich) 0.64 mg were dissolved per mL of ethylene glycol (EG). Then, chloroplatinic acid solution was added to the EG solution and reduced in an oil bath for 3 h at 150 °C while refluxing under N_2. After cooling to room temperature, alumina was introduced into the flask and refluxed at 100 °C overnight. The solution was washed in deionized water and dried in vacuum oven. Further details about catalytic reactions and characterizations can be found in Supplementary Information.

Ambient-pressure (AP) XPS measurements

AP-XPS experiments were conducted at the Pohang Accelerator Laboratory (PAL) and KAIST. At the 8A2 beamline at PAL, AP-XPS measurements were performed using a PHOIBOS 150 hemispherical electron analyzer (SPECS). A photon energy of 1050 eV was used to analyze the Ce 3*d* region (923-877 eV). The sample temperature was controlled with an IR laser and monitored via a thermocouple embedded in the sample holder. Details of the lab-based AP-XPS setup at KAIST can be found elsewhere[32]. The instrument at KAIST consisted of a monochromated Al Kα X-ray source (hν = 1486.74 eV) and a HiPP3 hemispherical electron analyzer (Scienta Omicron). Temperature was controlled using the resistive heating mode of HEAT3-PS equipment (Prevac). CO(g) and O_2(g) were introduced into the analysis chamber for the AP-XPS measurements. Peak analysis was carried out using CasaXPS software with an L Shirley background subtraction. All peaks were calibrated using the position of the Ce^{4+} $3d_{5/2}$ component (917.4 eV) as an internal reference. The Ce^{3+} area ratio was estimated by dividing the area of the Ce^{3+} peaks by the total area of all peaks.

O_2 uptake MD simulations

Molecular dynamics (MD) simulations were performed using the atomic simulation environment (ASE)[33] with the NVT ensemble, using a Berendsen thermostat with a temperature damping constant of 1 fs[34]. The temperature was maintained at a constant temperature of 773 K. For each model, we performed five statistically independent simulations with five different initial configurations of the O_2 environment for ensemble averaging to reduce statistical noise. All the results reported in this work are ensemble-averaged values from five MD simulations with uncertainties assessed by calculating the standard deviation from the ensemble average. The velocities of the system were initiated using the Maxwell-Boltzmann distribution and zeroed the total momentum to prevent drift. The simulations were conducted over 100,000 steps with a time step of 1 fs (100 ps in total). This duration was sufficient to achieve energy equilibrium, indicated by a rate of change of less than 0.0002 eV/ps. Additionally, the complete oxidation of the ceria domain was observed, confirming that the simulation time was adequate (Fig. 6d). All structure optimization relaxations were performed using the Broyden–Fletcher–Goldfarb–Shanno line search method[35]. All MD simulations were performed using the pretrained universal neural network potential (UNNP) software, preferred potential version 5.0.0 within the Matlantis distribution[36]. This UNNP was trained using an ab-initio database, achieving state-of-the-art accuracy in the Matbench benchmark[37]. Further details on the preparation of large-scale ceria domain models, the MD analysis method, and UNNP evaluation using density functional theory (DFT) calculations are presented in the supplementary information.

Data availability

The authors declare that the data supporting the findings of this study are available within the paper and its Supplementary Information files. Should any raw data files be needed in another format, they are available from the corresponding author upon request.

Code availability

All code and data supporting this study are openly available in Zenodo at https://doi.org/10.5281/zenodo.17446128. This includes computational scripts, input files, and processed data used to generate all figures and results presented in this manuscript.

References

1. Mars, P. & van Krevelen, D. W. Oxidations carried out by means of vanadium oxide catalysts. *Chem. Eng. Sci.* **3**, 41–59 (1954).
2. Batist, P. A., Der Kinderen, A. H. W. M., Leeuwenburgh, Y., Metz, F. A. M. G. & Schuit, G. C. A. The catalytic oxidation of 1-butene over bismuth molybdate catalysts: IV. Dependence of activity on the structures of the catalysts. *J. Catal.* **12**, 45–60 (1968).
3. Ricken, M., Nölting, J. & Riess, I. Specific heat and phase diagram of nonstoichiometric ceria (CeO_{2-x}). *J. Solid State Chem.* **54**, 89–99 (1984).
4. Yao, H. C. & Yao, Y. F. Y. Ceria in automotive exhaust catalysts: I. Oxygen storage. *J. Catal.* **86**, 254–265 (1984).
5. Masui, T., Ozaki, T., Machida, K.-I. & Adachi, G.-Y. Preparation of ceria–zirconia sub-catalysts for automotive exhaust cleaning. *J. Alloy. Comp.* **303–304**, 49–55 (2000).
6. Bruix, A. & Neyman, K. M. Modeling ceria-based nanomaterials for catalysis and related applications. *Catal. Lett.* **146**, 2053–2080 (2016).
7. Trovarelli, A. & Llorca, J. Ceria catalysts at nanoscale: how do crystal shapes shape catalysis? *ACS Catal.* **7**, 4716–4735 (2017).
8. Migani, A., Vayssilov, G. N., Bromley, S. T., Illas, F. & Neyman, K. M. Dramatic reduction of the oxygen vacancy formation energy in ceria particles: a possible key to their remarkable reactivity at the nanoscale. *J. Mater. Chem.* **20**, 10535–10546 (2010).
9. Muravev, V. et al. Size of cerium dioxide support nanocrystals dictates reactivity of highly dispersed palladium catalysts. *Science* **380**, 1174–1179 (2023).
10. Aneggi, E. et al. Ceria–zirconia particles wrapped in a 2D carbon envelope: improved low-temperature oxygen transfer and oxidation activity. *Angew. Chem. Inter. Ed.* **54**, 14040–14043 (2015).
11. Aneggi, E., Llorca, J., Boaro, M. & Trovarelli, A. Surface-structure sensitivity of CO oxidation over polycrystalline ceria powders. *J. Catal.* **234**, 88–95 (2005).
12. Vayssilov, G. N. et al. Support nanostructure boosts oxygen transfer to catalytically active platinum nanoparticles. *Nat. Mater.* **10**, 310–315 (2011).
13. Duprez, D., Descorme, C., Birchem, T. & Rohart, E. Oxygen storage and mobility on model three-way catalysts. *Top. Catal.* **16**, 49–56 (2001).
14. Hickey, N. et al. A comparative study of oxygen storage capacity over $Ce_{0.6}Zr_{0.4}O_2$ mixed oxides investigated by temperature-programmed reduction and dynamic OSC measurements. *Catal. Lett.* **72**, 45–50 (2001).
15. Aneggi, E., Boaro, M., De Leitenburg, C., Dolcetti, G. & Trovarelli, A. Insights into the redox properties of ceria-based oxides and their implications in catalysis. *J. Alloy. Comp.* **408-412**, 1096–1102 (2006).
16. Allian, A. D. et al. Chemisorption of CO and mechanism of CO oxidation on supported platinum nanoclusters. *J. Am. Chem. Soc.* **133**, 4498–4517 (2011).
17. Gänzler, A. M. et al. Unravelling the different reaction pathways for low temperature CO oxidation on Pt/CeO_2 and Pt/Al_2O_3 by spatially resolved structure-activity correlations. *J. Phys. Chem. Lett.* **10**, 7698–7705 (2019).
18. Zhang, Z. et al. Memory-dictated dynamics of single-atom Pt on CeO_2 for CO oxidation. *Nat. Commun.* **14**, 2664 (2023).
19. Nie, L. et al. Activation of surface lattice oxygen in single-atom Pt/CeO_2 for low-temperature CO oxidation. *Science* **358**, 1419–1423 (2017).
20. Pereira-Hernández, X. I. et al. Tuning Pt-CeO_2 interactions by high-temperature vapor-phase synthesis for improved reducibility of lattice oxygen. *Nat. Commun.* **10**, 1358 (2019).
21. Freund, H.-J., Meijer, G., Scheffler, M., Schlögl, R. & Wolf, M. CO Oxidation as a prototypical reaction for heterogeneous processes. *Angew. Chem. Int. Ed.* **50**, 10064–10094 (2011).
22. Zafiris, G. S. & Gorte, R. J. Evidence for a second CO Oxidation mechanism on Rh/Ceria. *J. Catal.* **143**, 86–91 (1993).
23. Cargnello, M. et al. Control of metal nanocrystal size reveals metal-support interface role for ceria catalysts. *Science* **341**, 771–773 (2013).
24. Lu, J.-Q., Sun, C.-X., Li, N., Jia, A.-P. & Luo, M.-F. Kinetic study of CO oxidation over CuO/MO_2 (M=Si, Ti and Ce) catalysts. *Appl. Surf. Sci.* **287**, 124–134 (2013).
25. DeRita, L. et al. Catalyst architecture for stable single atom dispersion enables site-specific spectroscopic and reactivity measurements of CO adsorbed to Pt atoms, oxidized Pt clusters, and metallic Pt clusters on TiO_2. *J. Am. Chem. Soc.* **139**, 14150–14165 (2017).
26. Pan, Z.-Z., Li, Y., Zhao, Y., Zhang, C. & Chen, H. Bulk phase charge transfer in focus—and in sequential along with surface steps. *Catal. Today* **364**, 2–6 (2021).
27. Kacimi, S., Barbier, J., Taha, R. & Duprez, D. Oxygen storage capacity of promoted Rh/CeC_2 catalysts. Exceptional behavior of $RhCu/CeO_2$. *Catal. Lett.* **22**, 343–350 (1993).
28. Lambrou, P. S., Costa, C. N., Christou, S. Y. & Efstathiou, A. M. Dynamics of oxygen storage and release on commercial aged Pd-Rh three-way catalysts and their characterization by transient experiments. *Appl. Catal. B Environ.* **54**, 237–250 (2004).

29. Sadokhina, N., Smedler, G., Nylén, U., Olofsson, M. & Olsson, L. Deceleration of SO_2 poisoning on $PtPd/Al_2O_3$ catalyst during complete methane oxidation. *Appl. Catal. B Environ.* **236**, 384–395 (2018).
30. Goodman, E. D. et al. Uniform Pt/Pd bimetallic nanocrystals demonstrate platinum effect on palladium methane combustion activity and stability. *ACS Catal.* **7**, 4372–4380 (2017).
31. Ding, C. et al. Reversible transformation and distribution determination of diverse Pt single-atom species. *J. Am. Chem. Soc.* **145**, 2523–2531 (2023).
32. Song, K. et al. Enhancing catalytic performance and hot electron generation through engineering metal-oxide and oxide-oxide interfaces. *Catal. Today* **425**, 114306 (2024).
33. Larsen, A. H. et al. The atomic simulation environment-a Python library for working with atoms. *J. Phys. Condens. Mat.* **29**, 273002 (2017).
34. Berendsen, H. J. C., Postma, J. P. M., Vangunsteren, W. F., Dinola, A. & Haak, J. R. Molecular-dynamics with coupling to an external bath. *J. Chem. Phys.* **81**, 3684–3690 (1984).
35. Schlegel, H. B. Optimization of equilibrium geometries and transition structures. *J. Comput. Chem.* **3**, 214–218 (1982).
36. Takamoto, S. et al. Towards universal neural network potential for material discovery applicable to arbitrary combination of 45 elements. *Nat. Commun.* **13**, 2991 (2022).
37. Dunn, A., Wang, Q., Ganose, A., Dopp, D. & Jain, A. Benchmarking materials property prediction methods: the Matbench test set and Automatminer reference algorithm. *Npj Comput. Mater.* **6**, 138 (2020).

Acknowledgements

This work was financially supported by the National Research Foundation of Korea (NRF-2021R1A3B1076715 and 2022R1A2C3004242) funded by the Ministry of Education, Science and Technology, Republic of Korea. The experiments at Pohang light source were supported in part by MSIT and POSTECH.

Author contributions

Y.C. and H.L. conceived the project. Y.C. synthesized the catalysts, ran the reactions, and performed all the gas-phase characterizations. S.C. and J.W.H. performed computational calculation. J.H., J.K., and J.Y.P. performed AP-XPS measurements. J.-E.H., H.J., and Y.K. helped the characterizations and catalytic reactions. Y.C., S.C., J.H., J.Y.P., J.W.H., and H.L. wrote the manuscript. All authors commented on the manuscript.

Competing interests

The authors declare no competing interests.

Additional information

Supplementary information The online version contains supplementary material available at https://doi.org/10.1038/s41467-025-66242-5.

Correspondence and requests for materials should be addressed to Jeong Young Park, Jeong Woo Han or Hyunjoo Lee.

Peer review information *Nature Communications* thanks Haichao Liu and the other anonymous reviewer(s) for their contribution to the peer review of this work. A peer review file is available.